ADVANCED FUNCTIONAL MATERIALS
www.afm-journal.de

Check for updates

Contact Engineering of Layered MoS_2 via Chemically Dipping Treatments

Seungho Bang, Sangyeob Lee, Amritesh Rai, Ngoc Thanh Duong, Iljo Kawk, Steven Wolf, Choong-Heui Chung, Sanjay K. Banerjee, Andrew C. Kummel, Mun Seok Jeong, and Jun Hong Park**

The performance of electronic/optoelectronic devices is governed by carrier injection through metal–semiconductor contact; therefore, it is crucial to employ low-resistance source/drain contacts. However, unintentional introduction of extrinsic defects, such as substoichiometric oxidation states at the metal–semiconductor interface, can degrade carrier injection. In this report, controlling the unintentional extrinsic defect states in layered MoS_2 is demonstrated using a two-step chemical treatment, $(NH_4)_2S(aq)$ treatment and vacuum annealing, to enhance the contact behavior of metal/MoS_2 interfaces. The two-step treatment induces changes in the contact of single layer MoS_2 field effect transistors from nonlinear Schottky to Ohmic behavior, along with a reduction of contact resistance from 35.2 to 5.2 kΩ. Moreover, the enhancement of I_{ON} and electron field effect mobility of single layer MoS_2 field effect transistors is nearly double for *n*-branch operation. This enhanced contact behavior resulting from the two-step treatment is likely due to the removal of oxidation defects, which can be unintentionally introduced during synthesis or fabrication processes. The removal of oxygen defects is confirmed by scanning tunneling microscopy and X-ray photoelectron spectroscopy. This two-step $(NH_4)_2S(aq)$ chemical functionalization process provides a facile pathway to controlling the defect states in transition metal dichalcogenides (TMDs), to enhance the metal-contact behavior of TMDs.

1. Introduction

Si-based complementary metal–oxide–semiconductors (CMOS) technology has driven the growth of the semiconductor industry due to its low fabrication cost and outstanding performance.[1] However, with the scaling of the channel length of Si field effect transistors (FETs) to a few nanometers, a fundamental limitation has arisen from the intrinsic challenges related to the 3D bulk body of the Si channel, such as power consumption and short channel effects.[2] Intrinsically atomic-thin channel materials have been proposed as ultrathin channel bodies to enhance the gate control and suppress short-channel leakage.[3] Coupling an intrinsically atomically thin body with a finite bandgap, layered transition metal dichalcogenides (TMDs) have been employed as semiconducting channel platforms with large ON/OFF ratio and near theoretical subthreshold swing.[3b,4] TMDs demonstrate a finite bandgap which spans from 0.9 to 2.5 eV; therefore, they have been studied as alternative semiconductor channels. Additionally, the band structure of TMD can be governed by controlling the number of layers or surface functionalization, while the mobility of TMDs is comparable to existing heavily doped thin Si channels;[5] therefore, the applications of TMDs can be expanded to logic devices and optoelectronics.[6]

Typically, the output performance of electronic/optoelectronic semiconductor devices can be altered by a change of

Dr. S. Bang, Dr. N. T. Duong, Prof. M. S. Jeong
Department of Energy Science
Sungkyunkwan University
Suwon 16419, Republic of Korea
E-mail: mjeong@skku.edu

Dr. S. Bang, Dr. N. T. Duong, Prof. M. S. Jeong
Center for Integrated Nanostructure Physics
Institute for Basic Science
Sungkyunkwan University
Suwon 16419, Republic of Korea

Prof. S. Lee, Prof. C.-H. Chung
Department of Materials Science and Engineering
Hanbat National University
Daejeon 34158, Republic of Korea

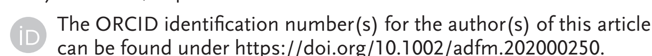
The ORCID identification number(s) for the author(s) of this article can be found under https://doi.org/10.1002/adfm.202000250.

DOI: 10.1002/adfm.202000250

Dr. A. Rai, Prof. S. K. Banerjee
Microelectronics Research Center
Department of Electrical and Computer Engineering
The University of Texas at Austin
Austin, TX 78758, USA

Dr. I. Kawk, Dr. S. Wolf
Materials Science and Engineering Program
University of California
San Diego La Jolla, CA 92093, USA

Prof. A. C. Kummel
Department of Chemistry and Biochemistry
University of California
San Diego La Jolla, CA 92093, USA

Prof. J. H. Park
School of Materials Science and Engineering
Gyeongsang National University
Jinju 52828, Republic of Korea
E-mail: yakte@gnu.ac.kr

© 2020 WILEY-VCH Verlag GmbH & Co. KGaA, Weinheim

resistance at the channel surface or the contact junctions.[7] To fabricate electronic and optoelectronic transistors, it is crucial to form low resistance metallic electrodes (source/drain) on semiconductor channels to inject the charge carriers through metal–semiconductor interfaces. Afterward, when a carrier pathway is opened by electrostatic gate control or optical stimulation, injected charge carriers are transported via the semiconductor channel. The charge transfer process and the carrier mobility values can be degraded by existence of resistance sources at the contact interfaces or near the metal–semiconductor interfaces,[7a,b,f] consistent with strong dependence of performance on existence of electrical resistance at the channel surfaces or metal–semiconductor interfaces.

One of known sources for resistances of the TMD devices is unintentional oxidation/interfacial states at the channel surface or contact interfaces formed during TMDs growth and the device fabrication process.[8] Typically, the growth of TMDs via chemical vapor deposition/transport (CVD) is initiated from the reduction of solid metal oxides (MO_x or WO_x) by reaction with elementary S or Se to induce the formation of crystalline TMDs.[9] The TMDs are transferred to ambient air for standard semiconductor devices fabrication processing.[10] It has been reported that the deposition of metal contacts on TMD surfaces in high vacuum (about 10^{-5}–10^{-7} Torr) involves the formation of metal oxide at the metal/TMDs interface due to metal–background gas reactions.[8a,b] Therefore, during these growth and fabrication processes, the defective metal oxides or byproducts including other possible contaminants (e.g., hydrocarbon) can be unintentionally introduced in the TMDs. These nonstoichiometric metal oxides can have dipoles and defect states near Fermi energy level; therefore, the carriers can be trapped or scattered by metal oxides located at the channel surfaces or at the metal/TMDs interfaces.[11] Moreover, existence of chemical disorder can induce the Fermi level pinning, consistent with degradation of contact performance.[12] Therefore, it is crucial to control the chemical states at the TMD surfaces and remove the defective states to enhance the electric and optical properties of TMDs. However, there are few reports of the selective removal of these oxides from TMDs without degradation of pristine TMDs crystallinity because the metal oxides at the TMDs are thermodynamically more stable than the crystalline TMDs.

In this report, an effective chemical method to remove MoO_x from layered MoS_2 surfaces leading to enhancement of electrical output performance is demonstrated. The present technique is composed of two steps: surface chemical reaction, using an $(NH_4)_2S$ (aq), and annealing in vacuum. Using scanning tunneling microscopy (STM) and spectroscopy (STS) of bulk MoS_2 before and after the two-step $(NH_4)_2S$ (aq) treatment is employed to elucidate the effects of treatment on atomic scale topographical and electronic properties of MoS_2. To track the chemical transition from the two-step treatment of MoS_2, X-ray photoelectron spectroscopy (XPS) is employed; both STM/STS and XPS results reveals that the oxidation states are removed after dipping MoS_2 into $(NH_4)_2S$ (aq) and vacuum annealing, while the crystal structure and Mo/S ratio of MoS_2 are maintained. As a result of the removal of oxygen defects by the two-step process on MoS_2, the Schottky contact behavior of bare single layer MoS_2 FETs with Au/Cr metal contact transitions to Ohmic contact behavior with a reduction of contact resistance by 6 X. Moreover, this two-step treatment induces mobility enhancement of MoS_2 by about 3 X, as well as an increase of 4 X in ON state driving current. That data is consistent with defect engineering via a simple and facile chemical treatment to enhance metal-TMDs contacts, thereby enabling relatively simple integration of this chemical functionalization into conventional semiconductor processing.

2. Result and Discussion

2.1. Raman and Photoluminescence Analysis of Two-Step Treated MoS_2

The process of two-step functionalization to enhance of the electronic performance of MoS_2 is described in the schematic diagram of **Figure 1**a. Commercially available $(NH_4)_2S$ is employed with dilution in H_2O to 20%; bare MoS_2 flakes are dipped in the $(NH_4)_2S$(aq) solution for 10 s, then the treated samples are washed for 60 s with isopropanol. Afterward, the samples are transferred to the vacuum for the annealing process. During the annealing process of treated MoS_2, the temperature is held at 473 K in the vacuum ($P < 5 \times 10^{-6}$ torr) and annealing duration is limited in 10 min.

To elucidate the effect of two-step treatment on MoS_2 flakes, CVD grown single layer MoS_2 is spectroscopically probed using Raman spectroscopy. As shown in Figure 1b, Raman spectroscopy of a bare CVD single layer MoS_2 sample is performed in ambient with excitation at 532 nm; two prominent vibrational modes can be observed at 384.8 and 402.9 cm^{-1}, referred as the in-plane vibrational mode E^1_{2g} and out-of-plane vibrational mode A_{1g} respectively, and the peak-to-peak distance is about 18.1 cm^{-1}, consistent with the Raman spectra of single layer MoS_2 in previous reports.[13] After the two-step treatment of single layer MoS_2, similar Raman vibration behavior can be observed as shown the red curve; the E^1_{2g} and A_{1g} peaks are detected at 384.7 and 402.7 cm^{-1} respectively and are at nearly identical positions to the peaks in the Raman spectra of bare MoS_2 ML. The peak-to-peak distance of the chemically treated MoS_2 ML is 17.9 cm^{-1} similar to the value of bare MoS_2 ML, indicating the present two-step treatment does not induce transformation of the crystal structure of single layer MoS_2.

The efficacy of exciton generation is improved with the present two-step treatment as determined by photoluminescence (PL) spectroscopy. As shown in Figure 1c, the change in PL of MoS_2 is tracked with constant laser power (1 mW) and wavelength on the same CVD single layer MoS_2 flake upon two-step treatment. Prior to $(NH_4)_2S$ treatment and annealing, the MoS_2 single layer has two prominent broad peaks at 672 nm and 628 nm, referred to as A and B respectively, consistent with previous reports.[14] The two major peaks, A and B, result from the spin-orbit splitting of the valence band in MoS_2 single layers. After the two-step treatment of the MoS_2 single layer sample, the intensity of both A and B peaks greatly increases as shown by the red curve. Although the position of PL peaks for treated MoS_2 ML are

© 2020 WILEY-VCH Verlag GmbH & Co. KGaA, Weinheim

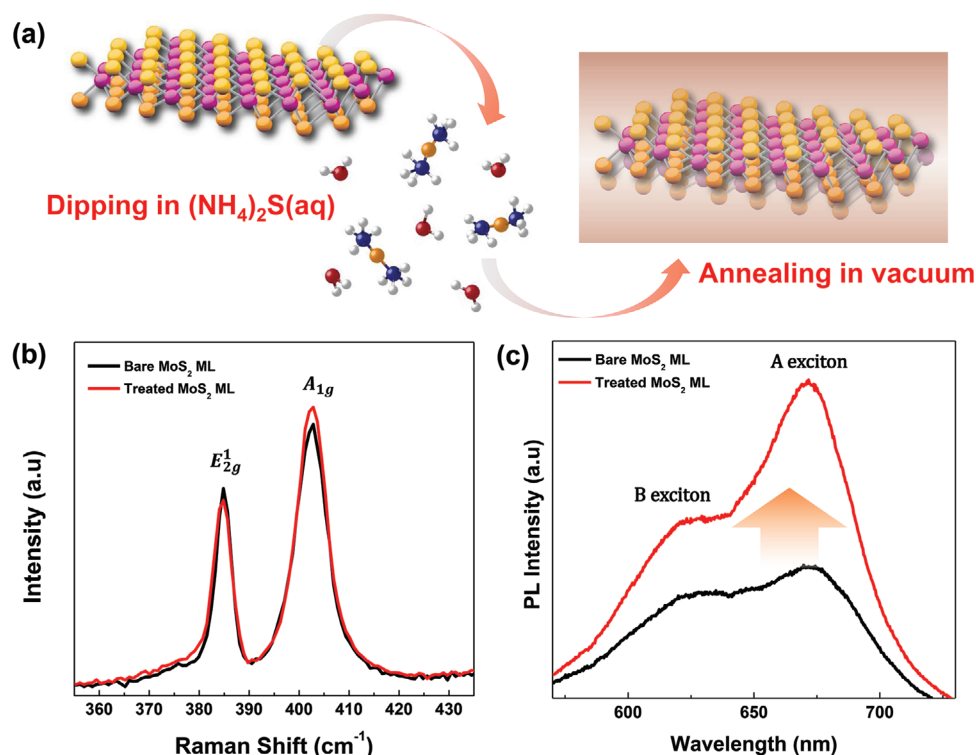

Figure 1. Raman and photoluminescence (PL) spectra of single layer MoS_2 before and after $(NH_4)_2S$(aq) chemical treatment and annealing at 473 K. a) Schematic diagram illustrating the two-step chemical treatment process, consisting of $(NH_4)_2S$(aq) treatment and followed annealing processes. b) Raman spectra of single layer MoS_2 with 532 nm laser excitation. c) PL spectra of single layer MoS_2 under a 532 nm laser excitation with 1 mW incident power.

nearly identical to the position of PL peaks for bare MoS_2 ML, the intensity of PL peak A increases 50% with chemical treatment, while the intensity of PL peak B is enhanced more than 100% with chemical treatment. The improvement of PL is consistent with an increase of quantum yield for exciton formation by removal optically unfavorable defects at the surface of MoS_2,[9c] which is confirmed below.

2.2. Electrical Characteristic of Two-Step Treated MoS_2: Transition of Contact Behavior

The electronic impact of two-step treatment to MoS_2 ML is elucidated by electronic characteristic of back-gated MoS_2 FETs at 300 K under vacuum (1×10^{-5} torr) in the absence of light. The back-gated FETs are fabricated with the CVD grown single layer MoS_2 on SiO_2/Si substrates. Once the MoS_2 single layer is located at the desired place on SiO_2/Si, the MoS_2 layer is trimmed to a rectangular shape (channel width of 3 µm) using electron beam lithography and SF_6 reactive etching. Afterward, Au/Cr pads (total thickness: 50 nm) are defined by electron-beam deposition (P: 1×10^{-6} torr) and lithographic patterning to carry out transfer length measurement (TLM), as shown in **Figure 2**a. The schematic diagram in Figure 2b reveals three different channel lengths, denoted as the L1 (1.68 µm), L2 (5.50 µm), and L3 (13.72 µm) channels; these are employed to determine the total resistance (R_T) between two successive metal contacts.

The transfer characteristics of channels L1, L2, and L3 are shown in Figure 2c with forward (negative to positive) and backward (positive to negative) sweeping of the back-gate bias V_{BG}, while the drain bias V_{DS} is kept at 0.01 V. As shown in the transfer curve of the single MoS_2 FETs, bare MoS_2 reveals n-dominant behavior for all channel L1, L2 and L3, consistent with typical single layer MoS_2 FETs.[3c,15] The measured transfer characteristic of two-step treated MoS_2 FETs is shown in the dotted curve; the position of back-gate voltage where the n-branch current starts to emerge is shifted toward negative V_{BG} values (about – 35 to – 39 V) after $(NH_4)_2S$(aq) chemical treatment, consistent with a negative threshold voltage shift. It is noted that to prevent the thermal damage during metal-MoS_2 contact formation, the annealing temperature is limited to 473 K. However, since elementary S is highly volatile in ambient due to formation of SO_x,[16] the impact of elementary S adlayer from $(NH_4)_2S$(aq) on the MoS_2 surface in electric enhancement of MoS_2 transistors can be considered to be negligible. Although I_{OFF} of L1, L2, and L3 is nearly constant, I_{ON} at the n-branch increases with negative shift of threshold voltage; therefore, the I_{ON}/I_{OFF} ratios between $V_{BG} = -60$ and +60 V of all treated channels are improved 4 X. It is noted that the present two-step treatment involves vacuum annealing at 473 K; therefore, it is hypothesized that molecular adsorbates, such as HS,[17] would be mostly removed from MoS_2 surface by annealing in vacuum. Moreover, NH_3 or H_2S have negligible effects on the electronic structure of TMDs as shown in previous report.[17] Since the Raman spectra in Figure 1b

© 2020 WILEY-VCH Verlag GmbH & Co. KGaA, Weinheim

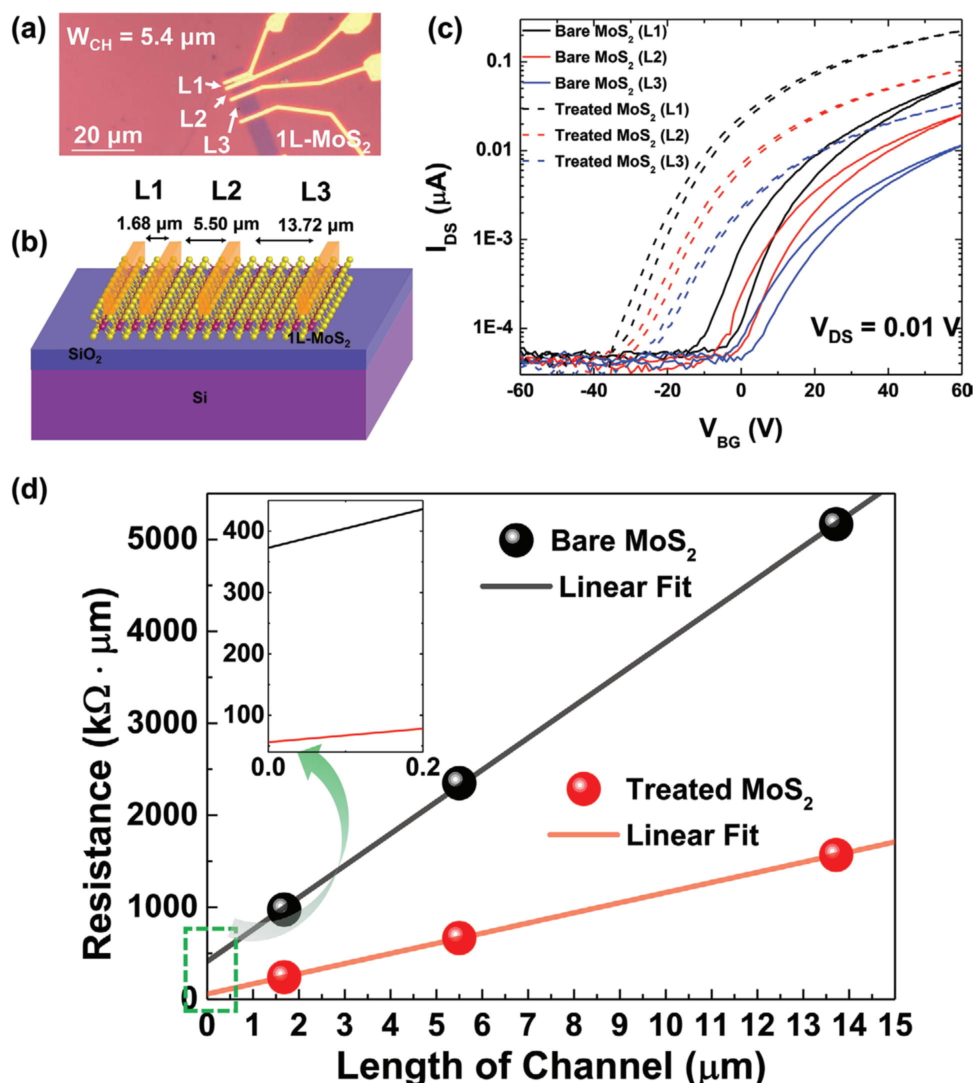

Figure 2. Transfer length measurement of single layer MoS_2 before and after $(NH_4)_2S$(aq) chemical treatment and annealing at 473 K. a) Optical image of TLM structure for MoS_2 with channel length L1, L2, and L3. It is noted that the channel width (W_{CH}) is 5.4 µm. b) Schematic illustration of the MoS_2 TLM FET. The channel lengths of L1, L2, and L3 are 1.68, 5.50, 13.72 µm, respectively. c) Back-gated transfer curves of channel L1, L2, and L3 in log scale. Solid curves correspond to bare single layer MoS_2, while dotted curves correspond to treated single layer MoS_2. d) Resistance versus channel lengths of single layer MoS_2 for Au/Cr contacts. The resistance of bare MoS_2 is shown as a black line, while the resistance of treated MoS_2 is shown as a red line. Inset is enlarged R_{TOT} versus L_{CH} near $L = 0$ to determine zero-distance contact resistance of MoS_2.

reveal that the two-step treatment does not induce structure changes in MoS_2, the shift of threshold voltage in Figure 2c is unlikely to be the result of surface or substitutional doping of MoS_2. Instead, improvement of carrier transport behavior with the two-step treatment is likely one of the sources of source of the threshold voltage shift, as shown in Figure S7 (Supporting Information). As a result of the improved ON/OFF ratio, the subthreshold swing (SS) below the V_{TH} are improved from 8.19 to 3.4 V dec^{-1} with the two-step chemical treatment.

The field effect mobility of electron ($\mu_{FE\text{-}e}$) is extracted using linear I–V transfer curves from the back-gated transistors, using Equation (1)

$$\mu_{FE\text{-}e} = \left(\delta I_{DS}/\delta V_{BG}\,|_{max}\right)\left(L/W\right)\left(1/C_{OX}\right)\left(1/V_{DS}\right) \quad (1)$$

where $\delta I_{DS}/\delta V_{BG}\,|_{max}$ is the maximum back-gated transconductance. L and W are the length and width of the channel, respectively. C_{OX} (= $\varepsilon_0 \cdot \varepsilon_r/d$; ε_r = 3.9) represents the back-gate capacitance of SiO_2 (285 nm). Using this equation, the $\mu_{FE\text{-}e}$ of the bare single layer MoS_2 FET is determined as 7.4–11.42 $cm^2\ V^{-1}\ s^{-1}$, while the $\mu_{FE\text{-}h}$ of treated single layer MoS_2 FET is estimated to be 13.6–17.69 $cm^2\ V^{-1}\ s^{-1}$, consistent with about over 60% enhancement in the electron mobility.

To elucidate the origin of enhancement in the electric performance of single layer MoS_2, total resistance (R_T) of MoS_2 as a function of channel length is determined using a TLM configuration. The total resistance (R_{TOT}) of bare single layer MoS_2 is plotted as a function of distance between electrodes in Figure 2d. After the two-step treatment of same MoS_2 FET, the

© 2020 WILEY-VCH Verlag GmbH & Co. KGaA, Weinheim

total resistance of treated MoS_2 at L1, L2, and L3 is reduced, as shown in the red line in Figure 2d. The contact resistance (R_C) of bare MoS_2 with Au/Cr contact is about 35 kΩ, while the R_C of treated MoS_2 with Au/Cr is determined to 5.2 kΩ, consistent with decreases of R_C by a factor of ≈6. Consequently, the present two-step treatment induces the improvement of carrier transfer behavior at the metal-MoS_2 channel contact junctions, resulting in reduction of contact resistance.

The reduction of contact resistance via the two-step treatment is confirmed with output characteristics curves with tracking of the degree of linearity in I_D–V_{DS}. All gate-dependent output characteristics in **Figure 3** are measured with same sweep rate 0.2 V s^{-1}. Figure 3a reveals that I_D is nonlinearly correlated with V_{DS}, consistent with a Schottky behavior of metal contacts on single layer MoS_2. For V_{BG} = 40 V, the output current (I_{ON}) is ≈3.2 µA, when V_{DS} is 1.0 V, consistent with the existence of n-branch Schottky barrier across the path from the metal pad to the single layer MoS_2 channel. Moreover, as V_{DS} is swept forward (negative to positive branch) and backward (positive to negative branch), a large hysteresis can be observed as shown in Figure 3b. It has been reported that the hysteresis of transistors originates from extrinsic defects, such as molecular adsorption on the semiconductor channel or sub-stoichiometric oxide/carbide in the channel because these "extrinsic defects" can act charge trapping/scattering centers[18] to degrade the efficiency of carrier injection over contact barriers. Conversely, as shown in Figure 3c, the two-step chemical treatment induces an increase of I_D by a factor of ≈3 X (I_{ON} ≈ 13 µA for V_{BG} = 40 V and V_{DS} = 1.0 V), and I_D linearly increases upon sweeping V_{DS} from negative to positive bias, consistent with near-Ohmic behavior of single layer MoS_2 FET. This significant improvement of contact behavior is consistent with the present two-step chemical treatment inducing the removal of oxidative defects access region of MoS_2 channel. This implies

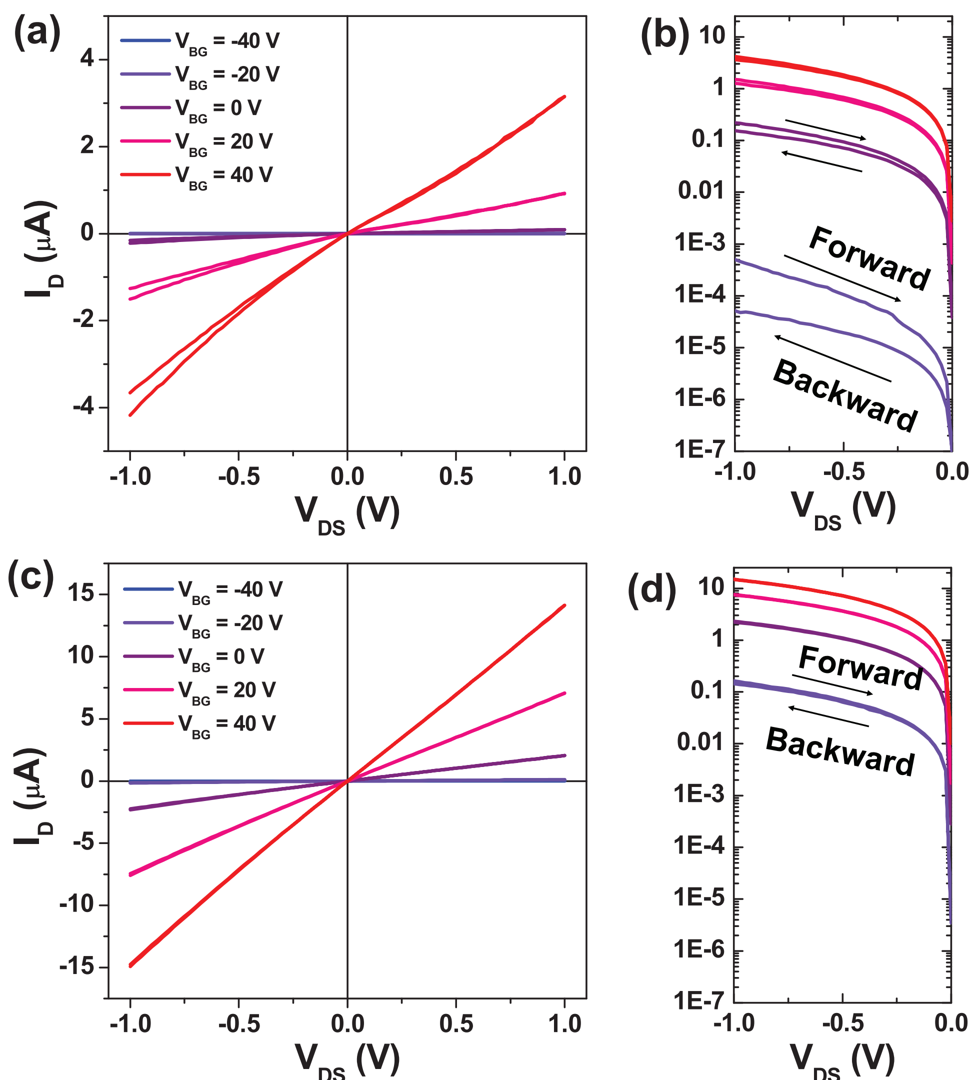

Figure 3. Output and hysteresis characteristic of bare single layer MoS_2 FET and treated single layer MoS_2 FET. a) Output characteristic of bare single layer MoS_2 FETs (channel L2 of Figure 4) with a linear scale. b) Expanded output characteristic plot of (a) from −1.0 to 0 V with a logarithmic scale. c) Output characteristic of treated single layer MoS_2 FET (L2) with a linear scale. d) Expanded output characteristic plot of (b) from −1.0 to 0 with a logarithmic scale.

© 2020 WILEY-VCH Verlag GmbH & Co. KGaA, Weinheim

that electron injection from the Au/Cr contacts into the MoS_2 is facilitated with removal of carrier trapping/scattering centers. The electric enhancement in MoS_2 FETs can be also confirmed with the significant reduction of hysteresis, as shown in Figure 3d; the removal of oxidative defects in MoS_2 results in facile electron transfer with suppression of carrier trapping/scattering near extrinsic defects.

2.3. Surface Chemistry of MoS_2 during Two-Step Treatment

To confirm that removal of oxidative defects is the origin of enhanced metal contact behavior of MoS_2 FETs with the present two-step $(NH_4)_2S$(aq) treatment, STM and STS are performed on the MoS_2 surface before and after $(NH_4)_2S$ treatment and annealing. Prior to treatment, two different areas of MoS_2 bulk are probed to verify the initial properties of MoS_2 surface. As shown in **Figure 4**a,b, two different types of defects are observed on bare surface of MoS_2 bulk at 2 V (empty states) and at −2 V (filled states); bright features (white circles) can be observed on the surfaces of MoS_2, while dark features (yellow circles) are detected with smaller density than white corrugation. The bright features are visible in both empty and filled state imaging modes, consistent with a structural protrusion, rather than an electronic effect. Previous reports reveal that the surface of MoS_2 with low defects density is typically smooth and atomically flat on various substrates, opposite to the present MoS_2 STM images. It is noted that previous reports reveal that metallic defects on MoS_2 are observed in only empty state or filled state imaging modes[19] and molecular adsorption on MoS_2 typically involves the dark circles surrounding the adsorbates, consistent with the electron depleted regions. Consequently, it is hypothesized that observed protrusions arise from the formation of extrinsic defects in synthesis or ambient conditions, rather than existence of metallic defects or adsorption defects.

After verification of MoS_2 surface using STM and STS, the two-step chemical treatment is performed with the same MoS_2 bulk sample. After dipping bulk MoS_2 in $(NH_4)_2S$(aq) at 300 K without annealing process, the large area empty state STM image in Figure 4c shows the surface of treated MoS_2 with horizontal noise;[20] this is consistent with weak interactions between molecular adsorbates and the STM metal tip at 100 K. The status of STM tip can be chemically and physically altered, resulting in STM tip noise along the scan direction. To elucidate the effect of aqueous $(NH_4)_2S$ treatment on the surface of MoS_2, excess adsorbates are removed from the MoS_2 by thermal annealing at 523 K for 5 min in the ultra high vacuum (UHV) chamber. As shown in Figure 4d, the flat surface of treated MoS_2 is shown without observation of white defects. After additionally annealing the same sample in the UHV chamber at 673 K, a hexagonal array of S atoms in MoS_2 surface is observed in an atomically resolved STM image (Figure 4e), consistent with the hexagonal pattern observed in the Fourier transform image of the inset; the interatomic distance of S atoms is about 0.33 ± 0.01 nm, which is consistent with previous reports.[21] The large area images with two different areas in the Supporting Information show that there are no “white protrusion” defects in the two-step treated MoS_2 surface and only dark metallic defects can be observed in two-step treated MoS_2.

The electronic structure transition of the MoS_2 surface upon chemical treatment and vacuum annealing is probed using STS. As shown in Figure 4f, the initial band structure is shown as a black curve; the measured bandgap is ≈1.2 eV with the Fermi level positioned near conduction band edge.[19a,22] After aqueous $(NH_4)_2S$ treatment, the bandgap is expanded about 1.8 eV and the Fermi level is positioned in the middle of bandgap. The expanded bandgap (≈1.8 eV) of the MoS_2 surface remains after UHV annealing at 523 K, while the Fermi level position is

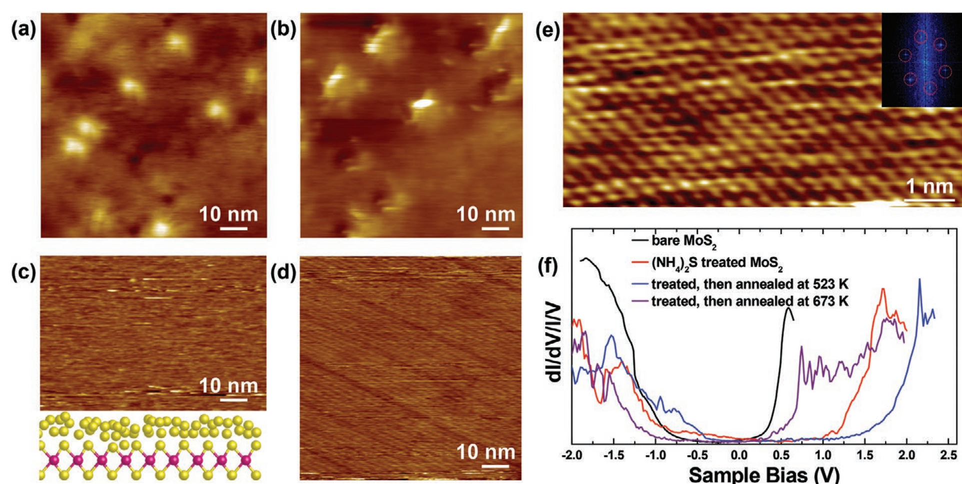

Figure 4. Scanning probe microscopy and spectroscopy of bulk MoS_2 before and after $(NH_4)_2S$ treatment and annealing processes. a) Empty state STM image of bare bulk MoS_2 ($V_S = 2$ V, $I_T = 40$ pA). b) Filled state STM image of bare bulk MoS_2 ($V_S = -2$ V, $I_T = 40$ pA). It is noted that STM images in (a) and (b) probe different areas on the same sample. c) Empty state STM image of $(NH_4)_2S$(aq) treated MoS_2 with no anneal ($V_S = 2$ V, $I_T = 20$ pA). d) Empty state STM image of $(NH_4)_2S$(aq) treated MoS_2, after annealing 473 K in the UHV chamber for 30 min ($V_S = 2$ V, $I_T = 20$ pA). e) Atomically resolved STM image of $(NH_4)_2S$(aq) treated MoS_2, after annealing 573 K in the UHV chamber for 30 min ($V_S = -0.8$ V, $I_T = 380$ pA). Inset displays the Fourier transform of the STM image. f) Local density of states (LDOS) of bulk MoS_2 surface probed via STS after two-step treatment. Each curve is averaged from five to seven individual STS curves.

© 2020 WILEY-VCH Verlag GmbH & Co. KGaA, Weinheim

Figure 5. XPS spectra of bulk MoS_2, before and after $(NH_4)_2S$(aq) chemical treatment and annealing at 423 K in UHV. The black curves correspond to the bare bulk MoS_2, and the red curves correspond to the annealed bulk MoS_2 without $(NH_4)_2S$(aq) treatment. Finally, the blue curves correspond to bulk MoS_2 after $(NH_4)_2S$(aq) treatment and followed annealing at 423 K for 30 min in UHV chamber. a) Spectra of Mo 3d. b) Spectra of S 2p. c) Spectra of O 1s. d) Schematic diagram shown the removal of partial oxidation states in MoS_2 with two-step treatments.

slightly shifted to valence band. It is known that the elementary S has a 1.65 eV bandgap;[23] therefore, it can be hypothesized that an S or S contained molecules adlayer exists on top of MoS_2 surface with $(NH_4)_2S$ treatment. However, after annealing at 673 K in UHV chamber, the measured bandgap of the treated MoS_2 surface decreases to ≈1.3 eV, consistent with removal of S adlayer from MoS_2 surface. Consequently, based on STM/STS results and previous reports, $(NH_4)_2S$ in H_2O is expected to be dissociated into NH_3, HS, and H_2S as the follow chemical reactions[24]

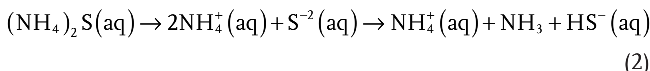

$$(NH_4)_2S(aq) \rightarrow 2NH_4^+(aq) + S^{-2}(aq) \rightarrow NH_4^+(aq) + NH_3 + HS^-(aq) \quad (2)$$

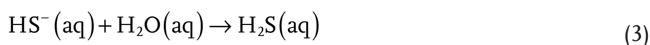

$$HS^-(aq) + H_2O(aq) \rightarrow H_2S(aq) \quad (3)$$

Therefore, it is hypothesized that NH_3, NH_4^+, H_2S, or HS^- adsorbs on the MoS_2 surface during $(NH_4)_2S$ dipping treatment. In second stage of the two-step treatment, $(NH_4)_2S$(aq) treated MoS_2 is annealed above 473 K in vacuum chamber; therefore, the adsorbates can react with MoO_x in MoS_2, consistent with thermally activated chemical reaction with following possible reactions

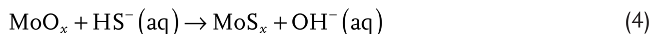

$$MoO_x + HS^-(aq) \rightarrow MoS_x + OH^-(aq) \quad (4)$$

$$MoS_x + heat \rightarrow MoS_2 \quad (5)$$

Or

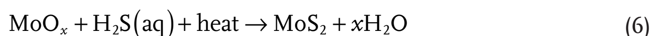

$$MoO_x + H_2S(aq) + heat \rightarrow MoS_2 + xH_2O \quad (6)$$

It is noted that this is speculative,[25] and DFT modeling is required for determination of a realistic mechanism.

To track the chemical change in bulk MoS_2 after two-step treatment, the surface of MoS_2 is probed using X-ray photoelectron spectroscopy (XPS). The spectra of Mo 3d and S 2p for bare bulk MoS_2, annealed MoS_2, and the two-step treated is shown in **Figure** 5a,b, respectively; there is negligible change in the position, width and intensity of each peaks. Furthermore, the atomic ratio of elementary S 2p to Mo 3d in the two-step treated bulk MoS_2 (2.32:1) is found to be nearly identical to S 2p/Mo 3d ratio of bare bulk MoS_2 (2.51:1) and annealed bulk MoS_2 (2.50:1), consistent with the absence of change of the chemical composition and binding configuration of the atoms in MoS_2 with the two-step

 © 2020 WILEY-VCH Verlag GmbH & Co. KGaA, Weinheim

treatment. It is noted that the precision of elementary ratio can be variable by a few percent, depending on the sample surfaces status.[26]

The chemical transition of oxygen in MoS_2 upon two-step treatment can be observed in the XPS spectra and compared to bare and annealed MoS_2 samples. As shown in Figure 5c, the XPS spectra of bare MoS_2 (the black curve) reveals a broad O1s peak in the range from 528 to 534 eV. After annealing the bare MoS_2 sample in UHV chamber at 523 K, a broad O 1s peak is detected as shown by the red curve. It can be hypothesized that the broad peak of O1s is consistent with the existence of multiple chemical configurations of oxygen in MoS_2. Based on the previous reports, adsorption of O on MoS_2 is observed around 531 eV,[27] and the O single in MoO_x has been observed in the range from 529 to 532 eV.[8b,28] It is noted that the origin for O in bare and annealed MoS_2 is not clear, but it can be assumed that O associated defects in MoS_2 are formed when the MoS_2 samples are stored in ambient air. However, after the two-step chemical treatments, the blue curve in Figure 2c shows the disappearance of O signal in the range from 536 to 528 eV. Therefore, it can be concluded that the $(NH_4)_2S$ treatment and annealing process induces near-completed removal of oxygen from MoS_2. As a result of removal of oxidative defects from MoS_2, the carrier transport behavior is enhanced with transition from Schottky behavior to Ohmic behavior of metal-MoS_2 contact, confirmed by electric characteristic of Figures 2 and 3.

3. Conclusion

The two-step chemical treatment of layered MoS_2 using $(NH_4)_2S$(aq) is demonstrated to enhance the contact behavior of metal/TMDs via controlling the unintentional extrinsic defect states. Using STM/STS, sequent observation of the MoS_2 surface at molecular level upon chemical treatment reveals that the defect states, which are shown as bright protrusions in both empty and filled states, are nearly completely removed by dipping in $(NH_4)_2S$(aq) and annealing at 523 K in vacuum, without inducing atomic structural damage in MoS_2. This removal of oxygen defects can be confirmed by XPS results; after two-step treatment, Mo/S ratio is nearly constant, while the oxygen signal completely disappears, consistent with removal of oxygen species in MoS_2. These oxidative defects can be introduced in MoS_2 during the synthesis process of MoS_2 or the fabrication processes in ambient conditions; therefore, it is hypothesized that these defect states can degrade electric performance of MoS_2 FETs with act as trapping/scattering center for carrier. However, as a result of the removal of unintentional oxygen defects from MoS_2, the optical and electronic performance of single layer MoS_2 is significantly enhanced. The PL intensity of single layer MoS_2 is doubled with chemical treatment, consistent with improvement of quantum yield for exciton formation by removal oxidation defects at the surface of MoS_2. Moreover, as the contact behavior changes from nonlinear Schottky behavior to nearly linear Ohmic behavior in output I_D versus V_{DS} characteristic of single layer MoS_2 FET, the contact resistance of Au/Cr/MoS_2 junction decreases from 35 to 5.2 kΩ, indicating facilitated injection of electron from metal pads to MoS_2 channels. As a result, the n-branch I_{ON} increases 3 X, and the electron field effect mobility is enhanced up to 3 X. Therefore, this two-step $(NH_4)_2S$(aq) chemical functionalization process provides a facile pathway to engineering the surface defect states in atomically thin TMDs to tune the contact behavior of metal/semiconducting TMD junctions.

4. Experimental Section

Device Fabrication Process, Chemical Treatment Method, and Electrical & Optical Characterization: The CVD-grown single layer MoS_2 flakes were transferred using a wet transfer method on a SiO_2/Si substrate. The average flake size was 50 µm × 50 µm as observed by OM. E-beam lithography was employed to make the open area for deposition of Cr (5 nm/Au 50 nm), which was deposited using an E-beam evaporation system. For exact electrical characteristics of MoS_2 back-gate transistors, single layer MoS_2 flakes were etched to a rectangular shape using SF_6 (20 sccm, 20 s, 20 W) and O_2 (15 sccm, 15 s, 15 W) plasma. Finally, the back-gated MoS_2 FET was fabricated. After electrical measurements, the MoS_2 FET samples were fully dipped in the $(NH_4)_2S$(aq) solution for a specific time period, following which the samples were rinsed in IPA and dried by N_2 gas. The electrical properties were measured by a vacuum probe system (4200, Keithley) at high vacuum ($\approx 10^{-6}$ Torr). For Optical properties, PL and Raman measurements were performed by an optical microscope system (NTEGRA Spectra, NT-MDT) using a 532 nm laser with high magnification objective lens (100×, NA = 0.7). The gratings with 150 and 1800 grooves were used for PL and Raman, respectively.

STM/STS Method: Bulk MoS_2 purchased from SPI supplies (Structure Probe, Inc.) was mechanically exfoliated multiple times in ambient conditions to obtain clean surface. The bulk MoS_2 was transferred to an Omicron multipurpose UHV chamber ($<2 \times 10^{-10}$ torr). For STM/STS experiments, MoS_2 samples were annealed in UHV at 737 K for 30 min to remove the possible ambient contaminants or adsorbates, such as hydrocarbon, H_2O or CO. For STM/STS experiments, the samples were transferred into Omicron VT STM chamber without exposure to ambient air. All STM/STS experiments were carried out using electrochemically etched tungsten tips.

Supporting Information

Supporting Information is available from the Wiley Online Library or from the author.

Acknowledgements

This work was supported by NSF Grants DMR 1207213, DMR1400432, and EFRI-2DARE 1433490, and by LEAST-STARnet, a Semiconductor Research Corporation program, sponsored by MARCO and DARPA and by SRC NRI SWAN. This work was also supported by the National Research Foundation of Korea (NRF) grant funded by the Korea government (MSIT) (Nos. NRF-2018R1C1B5085644 and NRF-2019R1A2B5B02070657).

Conflict of Interest

The authors declare no conflict of interest.

Keywords

contact engineering, oxide defects, surface science, transition metal dichalcogenides, two-step chemical functionalization

Received: January 10, 2020
Revised: February 9, 2020
Published online: February 25, 2020

© 2020 WILEY-VCH Verlag GmbH & Co. KGaA, Weinheim

[1] a) A. D. Franklin, *Science* **2015**, *349*, aab2750; b) T. Sakurai, *IEICE Trans. Electron.* **2004**, *E87c*, 429.
[2] a) M. Luisier, M. Lundstrom, D. A. Antoniadis, J. Bokor, *IEEE Int. Electron Devices Meet.* **2011**, *11*, 2.1; b) E. Suzuki, K. Ishii, S. Kanemaru, T. Maeda, T. Tsutsumi, T. Sekigawa, K. Nagai, H. Hiroshima, *IEEE Trans. Electron Devices* **2000**, *47*, 354.
[3] a) M. Chhowalla, D. Jena, H. Zhang, *Nat. Rev. Mater.* **2016**, *1*, 16052; b) D. Sarkar, X. J. Xie, W. Liu, W. Cao, J. H. Kang, Y. J. Gong, S. Kraemer, P. M. Ajayan, K. Banerjee, *Nature* **2015**, *526*, 91; c) B. Radisavljevic, A. Radenovic, J. Brivio, V. Giacometti, A. Kis, *Nat. Nanotechnol.* **2011**, *6*, 147.
[4] S. B. Desai, S. R. Madhvapathy, A. B. Sachid, J. P. Llinas, Q. X. Wang, G. H. Ahn, G. Pitner, M. J. Kim, J. Bokor, C. M. Hu, H. S. P. Wong, A. Javey, *Science* **2016**, *354*, 99.
[5] a) D. Kim, H. Du, T. Kim, S. Shin, S. Kim, M. Song, C. Lee, J. Lee, H. Cheong, D. H. Seo, S. Seo, *AIP Adv.* **2016**, *6*, 105307; b) V. Podzorov, M. E. Gershenson, C. Kloc, R. Zeis, E. Bucher, *Appl. Phys. Lett.* **2004**, *84*, 3301.
[6] a) T. Cheiwchanchamnangij, W. R. L. Lambrecht, *Phys. Rev. B* **2012**, *85*, 205302; b) Y. Zhang, T. R. Chang, B. Zhou, Y. T. Cui, H. Yan, Z. K. Liu, F. Schmitt, J. Lee, R. Moore, Y. L. Chen, H. Lin, H. T. Jeng, S. K. Mo, Z. Hussain, A. Bansil, Z. X. Shen, *Nat. Nanotechnol.* **2014**, *9*, 111; c) P. C. Yeh, W. C. Jin, N. Zaki, D. T. Zhang, J. T. Liou, J. T. Sadowski, A. Al-Mahboob, J. I. Dadap, I. P. Herman, P. Sutter, R. M. Osgood, *Phys. Rev. B* **2015**, *91*, 041407(R).
[7] a) J. Bardeen, *Phys. Rev.* **1947**, *71*, 717; b) H. Hasegawa, T. Sawada, *Thin Solid Films* **1983**, *103*, 119; c) W. Liu, J. Kang, D. Sarkar, Y. Khatami, D. Jena, K. Banerjee, *Nano Lett.* **2013**, *13*, 1983; d) S. Chuang, C. Battaglia, A. Azcatl, S. McDonnell, J. S. Kang, X. Yin, M. Tosun, R. Kapadia, H. Fang, R. M. Wallace, A. Javey, *Nano Lett.* **2014**, *14*, 1337; e) J. Kang, W. Liu, D. Sarkar, D. Jena, K. Banerjee, *Phys. Rev. X* **2014**, *4*, 031005; f) R. T. Tung, *Appl. Phys. Rev.* **2014**, *1*, 011304; g) Y. Liu, J. Guo, E. Zhu, L. Liao, S. J. Lee, M. Ding, I. Shakir, V. Gambin, Y. Huang, X. Duan, *Nature* **2018**, *557*, 696.
[8] a) S. McDonnell, C. Smyth, C. L. Hinkle, R. M. Wallace, *ACS Appl. Mater. Interfaces* **2016**, *8*, 8289; b) C. M. Smyth, R. Addou, S. McDonnell, C. L. Hinkle, R. M. Wallace, *J. Phys. Chem. C* **2016**, *120*, 14719; c) C. M. Smyth, R. Addou, S. McDonnell, C. L. Hinkle, R. M. Wallace, *2D Mater.* **2017**, *4*, 025084.
[9] a) K. H. Zhang, S. M. Feng, J. J. Wang, A. Azcatl, N. Lu, R. Addou, N. Wang, C. J. Zhou, J. Lerach, V. Bojan, M. J. Kim, L. Q. Chen, R. M. Wallace, M. Terrones, J. Zhu, J. A. Robinson, *Nano Lett.* **2016**, *16*, 2125; b) M. H. Chiu, C. D. Zhang, H. W. Shiu, C. P. Chuu, C. H. Chen, C. Y. S. Chang, C. H. Chen, M. Y. Chou, C. K. Shih, L. J. Li, *Nat. Commun.* **2015**, *6*, 7666; c) H. Yao, L. Liu, Z. Wang, H. Li, L. Chen, M. E. Pam, W. Chen, H. Y. Yang, W. Zhang, Y. Shi, *Nanoscale* **2018**, *10*, 6105.
[10] a) S. H. Chae, Y. Jin, T. S. Kim, D. S. Chung, H. Na, H. Nam, H. Kim, D. J. Perello, H. Y. Jeong, T. H. Ly, Y. H. Lee, *ACS Nano* **2016**, *10*, 1309; b) J. H. Park, S. Vishwanath, X. Y. Liu, H. W. Zhou, S. M. Eichfeld, S. K. Fullerton-Shirey, J. A. Robinson, R. M. Feenstra, J. Furdyna, D. Jena, H. G. Xing, A. C. Kummel, *ACS Nano* **2016**, *10*, 4258; c) J. H. Park, S. Vishwanath, S. Wolf, K. H. Zhang, I. Kwak, M. Edmonds, M. Breeden, X. Y. Liu, M. Dobrowolska, J. Furdyna, J. A. Robinson, H. G. Xing, A. C. Kummel, *ACS Appl. Mater. Interfaces* **2017**, *9*, 29255.
[11] W. Goes, Y. Wimmer, A. M. El-Sayed, G. Rzepa, M. Jech, A. L. Shluger, T. Grasser, *Microelectron. Reliab.* **2018**, *87*, 286.
[12] A. Agrawal, J. Lin, M. Barth, R. White, B. Zheng, S. Chopra, S. Gupta, K. Wang, J. Gelatos, S. E. Mohney, S. Datta, *Appl. Phys. Lett.* **2014**, *104*, 112101.
[13] a) G. Kukucska, J. Koltai, *Phys. Status Solidi B* **2017**, *254*, 1700184; b) C. Lee, H. Yan, L. E. Brus, T. F. Heinz, J. Hone, S. Ryu, *ACS Nano* **2010**, *4*, 2695; c) G. L. Frey, R. Tenne, M. J. Matthews, M. S. Dresselhaus, G. Dresselhaus, *Phys. Rev. B* **1999**, *60*, 2883.
[14] a) K. F. Mak, K. L. He, C. Lee, G. H. Lee, J. Hone, T. F. Heinz, J. Shan, *Nat. Mater.* **2013**, *12*, 207; b) Z. Y. Yin, H. Li, H. Li, L. Jiang, Y. M. Shi, Y. H. Sun, G. Lu, Q. Zhang, X. D. Chen, H. Zhang, *ACS Nano* **2012**, *6*, 74.
[15] a) A. Sanne, R. Ghosh, A. Rai, M. N. Yogeesh, S. H. Shin, A. Sharma, K. Jarvis, L. Mathew, R. Rao, D. Akinwande, S. Banerjee, *Nano Lett.* **2015**, *15*, 5039; b) X. F. Li, L. M. Yang, M. W. Si, S. C. Li, M. Q. Huang, P. D. Ye, Y. Q. Wu, *Adv. Mater.* **2015**, *27*, 1547.
[16] a) W.-F. Sye, W.-S. Jou, *J. Chin. Chem. Soc.* **1993**, *40*, 455; b) Y. Li, L.-J. Wang, H.-L. Fan, J. Shangguan, H. Wang, J. Mi, *Energy Fuels* **2015**, *29*, 298.
[17] J. H. Park, A. Rai, J. Hwang, C. Zhang, I. Kwak, S. F. Wolf, S. Vishwanath, X. Liu, M. Dobrowolska, J. Furdyna, H. G. Xing, K. Cho, S. K. Banerjee, A. C. Kummel, *ACS Nano* **2019**, *13*, 7545.
[18] a) N. Liu, J. Baek, S. M. Kim, S. Hong, Y. K. Hong, Y. S. Kim, H.-S. Kim, S. Kim, J. Park, *ACS Appl. Mater. Interfaces* **2017**, *9*, 42943; b) H. Shimauchi, Y. Ohno, S. Kishimoto, T. Mizutani, *Jpn. J. Appl. Phys.* **2006**, *45*, 5501; c) D. J. Late, B. Liu, H. S. S. R. Matte, V. P. Dravid, C. N. R. Rao, *ACS Nano* **2012**, *6*, 5635; d) T. Li, G. Du, B. S. Zhang, Z. M. Zeng, *Appl. Phys. Lett.* **2014**, *105*, 093107.
[19] a) S. McDonnell, R. Addou, C. Buie, R. M. Wallace, C. L. Hinkle, *ACS Nano* **2014**, *8*, 2880; b) X. L. Liu, I. Balla, H. Bergeron, M. C. Hersam, *J. Phys. Chem. C* **2016**, *120*, 20798.
[20] a) R. Otero, F. Hummelink, F. Sato, S. B. Legoas, P. Thostrup, E. Laegsgaard, I. Stensgaard, D. S. Galvao, F. Besenbacher, *Nat. Mater.* **2004**, *3*, 779; b) H. L. Tierney, C. E. Calderon, A. E. Baber, E. C. H. Sykes, F. Wang, *J. Phys. Chem. C* **2010**, *114*, 3152; c) K. Ingo, S. Benjamin, K. Christian, *New J. Phys.* **2016**, *18*, 113022.
[21] a) C. D. Zhang, A. Johnson, C. L. Hsu, L. J. Li, C. K. Shih, *Nano Lett.* **2014**, *14*, 2443; b) X. L. Liu, I. Balla, H. Bergeron, G. P. Campbell, M. J. Bedzyk, M. C. Hersam, *ACS Nano* **2016**, *10*, 1067; c) X. D. Zhou, K. Kang, S. Xie, A. Dadgar, N. R. Monahan, X. Y. Zhu, J. Park, A. N. Pasupathy, *Nano Lett.* **2016**, *16*, 3148.
[22] a) A. Kumar, P. K. Ahluwalia, *Eur. Phys. J. B* **2012**, *85*, 186; b) J. Gusakova, X. Wang, L. L. Shiau, A. Krivosheeva, V. Shaposhnikov, V. Borisenko, V. Gusakov, B. K. Tay, *Phys. Status Solidi A* **2017**, *214*, 1700218.
[23] G. Liu, P. Niu, L. Yin, H.-M. Cheng, *J. Am. Chem. Soc.* **2012**, *134*, 9070.
[24] a) J. J. Senkevich, G. R. Yang, T. M. Lu, *Colloids Surf., A* **2003**, *214*, 119; b) S. L. Heslop, L. Peckler, A. J. Muscat, *J. Vac. Sci. Technol., A* **2017**, *35*, 03E110.
[25] a) P. R. Westmoreland, J. B. Gibson, D. P. Harrison, *Environ. Sci. Technol.* **1977**, *11*, 488; b) A. Davydov, K. T. Chuang, A. R. Sanger, *J. Phys. Chem. B* **1998**, *102*, 4745; c) J. A. Rodriguez, S. Chaturvedi, M. Kuhn, J. Hrbek, *J. Phys. Chem. B* **1998**, *102*, 5511; d) C. L. Carnes, K. J. Klabunde, *Chem. Mater.* **2002**, *14*, 1806; e) M.-Y. Jia, B. Xu, X.-L. Ding, S.-G. He, M.-F. Ge, *J. Phys. Chem. C* **2012**, *116*, 24184; f) M.-Y. Jia, X.-L. Ding, S.-G. He, M.-F. Ge, *J. Phys. Chem. A* **2013**, *117*, 8377.
[26] A. Proctor, P. M. A. Sherwood, *Anal. Chem.* **1982**, *54*, 13.
[27] a) D. Ganta, S. Sinha, R. T. Haasch, *Surf. Sci. Spectra* **2014**, *21*, 19; b) X. Yang, W. Fu, W. Liu, J. Hong, Y. Cai, C. Jin, M. Xu, H. Wang, D. Yang, H. Chen, *J. Mater. Chem. A* **2014**, *2*, 7727.
[28] a) J. G. Choi, L. T. Thompson, *Appl. Surf. Sci.* **1996**, *93*, 143; b) T. Schroeder, J. Zegenhagen, N. Magg, B. Immaraporn, H. J. Freund, *Surf. Sci.* **2004**, *552*, 85; c) X. Wang, Y. Xiao, J. Wang, L. Sun, M. Cao, *J. Power Sources* **2015**, *274*, 142.

© 2020 WILEY-VCH Verlag GmbH & Co. KGaA, Weinheim